
PHYSICS OF EARTH, ATMOSPHERE,
AND HYDROSPHERE

Modeling the Problem of Low-Orbital Satellite UV-Tomography of the Ionosphere

I. A. Nesterov*, A. M. Padokhin**, E. S. Andreeva, and S. A. Kalashnikova

Department of Physics, Moscow State University, Moscow, 119991 Russia

*e-mail: *nia2002@yandex.ru, **padokhin@physics.msu.ru*

Received December 2, 2015; in final form, January 14, 2016

Abstract—The results of modeling the direct and inverse problems of low-orbital satellite ultraviolet (UV) tomography of the ionospheric 135.6 OI volume emission rate are presented. The direct problem was solved with the orbital geometry of DMSP block 5D3 satellites with SSUSI and SSULI UV spectrographs among the other payloads, the real operating parameters of these instruments (the scan rate and the interval of scan angles), and the set of the model distributions of the volume emission rate that contain irregularities on various scales. The solution of the direct problem yields the radiation intensities in the 135.6 nm line, which is used as the input data for reconstructing the initial (prototype) model distributions of the volume emission rates. The obtained system of linear equations (SLE) was solved using the Algebraic Reconstruction Technique (ART) and Simultaneous Iterative Reconstructive Technique (SIRT) algorithms, which are highly efficient in problems of the low-orbit radio tomography of the ionosphere. It is shown that the initial model distribution can be successively reconstructed if one takes the non-negativity condition of the solution into account, uses weighting functions to decrease the solution in the regions where it is known to be a priori small, and applies inter-iteration smoothing to eliminate the effects of the approximation errors. Here, the averaging parameters should decrease in the course of the iterations. With these constraints fulfilled, the computational costs of the ART- and SIRT-based solutions are similar, while the reconstruction error is approximately 6%. The influence of random errors and bias in the data on the results of the reconstruction is explored. It is shown that with a given error level of the initial data the parameters of the reconstruction algorithms can be adjusted in such a way as to efficiently suppress the influence of the noise with a relative amplitude of 2–3% on the solution.

Keywords: ionosphere, tomography, UV radiation, modeling.

DOI: 10.3103/S0027134916030103

INTRODUCTION

The possibility of using the ultraviolet (UV) and visible wavelength airglow to study the electron and O^+ ion distributions in the F -region ionosphere was described at the end of the 1960s and beginning of the 1970s. Measurements in the visible band were carried out from the ground [1, 2], while in the UV band they were performed from spacecraft [3, 4]. These experiments revealed two possible mechanisms of the UV airglow: by the radiative recombination of O^+ ions and electrons and by oxygen ion–ion (O^+ and O^-) neutralization [5]; the airglow emission at 91.1 nm is exclusively driven by the radiative recombination reaction [6]. Later measurements in the mid-latitudes [7] supported the idea that radiative recombination is also the predominant mechanism of the 135.6 nm emission.

The use of the oxygen lines in the nightglow emission for the remote sensing of the electron concentration in the F -layer ionosphere was described in [8, 9]. The successful retrieval of electron density profiles from UV spectroscopy data was demonstrated in [9]

based on the 91.1 and 135.6 nm emissions data from the Low-resolution Airglow and Aurora Spectrograph (LORAAS) onboard the ARGOS satellite.

In the past decade, tomographic methods have come to be widely used for reconstructing the two-dimensional (2D) and three-dimensional (3D) distributions of the electron density in the ionosphere from the satellite UV spectroscopy data [10–13]. All these approaches have two features in common. First, they all use the next generation of UV spectrographs, such as the Global Ultraviolet Imager (GUVI) onboard the TIMED spacecraft and the Special Sensor Ultraviolet Spectrographic Imager (SSUSI) and Spectral Sensor Ultraviolet Limb Imager (SSULI) onboard the DMSP 5D3 satellites. As well, they all share the Chapman layer assumption for the approximation of the vertical profile of electron density, require additional information on ionospheric photochemistry, and use simple algebraic reconstruction algorithms, such as ART and MART, for solving the corresponding systems of linear equations (SLEs) of the problem. All

these factors restrict the quality of the resulting reconstructions. Therefore, in the past few years it has come to be more common to solve the problem of tomographic reconstruction of the volume emission rate at a selected wavelength in the ionosphere and thus to avoid specifying the particular physical mechanisms that produce the observed emission. Our present paper addresses this problem. Here, we model and optimize the algorithms for low-orbiting satellite UV tomography for reconstructing the volume emission rate of the ionospheric OI 135.6 nm emission with the real orbital geometry of the DMSP 5D3 satellites and the real operating parameters of the SSUSI and SSULI instruments.

1. THE INSTRUMENTS AND ORBITAL PARAMETERS

The next-generation American DMSP 5D3 satellites with SSUSI and SSULI spectral imagers began to be launched in 2003. To date, four satellites have been launched, with the last launch occurring in April 2014. The satellites fly at ~850 km above the Earth's surface in almost circular orbits that are solar synchronized and have high inclination (~99°).

The first instrument whose parameters are used in our modeling is the SSULI UV spectrograph that was designed at the Naval Research Laboratory. This instrument makes limb observations of the UV radiation in the spectral band from 80 to 170 nm with a resolution of 1.5 nm. SSUSI scans the Earth's atmosphere along the satellite track at a 90-s scan cadence in the angle sector from 10° to 27° below the satellite horizon.

As the second data source for our modeling, we used the SSUSI UV spectral imager developed at the John Hopkins University Applied Physics Laboratory (JHU APL). SSUSI provides cross-track line scanning in the far ultraviolet band and measures the emissions from five wavelength intervals: the 121.6 nm H⁺ line, O⁺ 130.4 and 135.6 nm lines, and two N₂ Lyman–Birge–Hopfield bands (140–150 and 165–180 nm). Each scan yields two profiles of the airglow radiation, one in the limb-viewing section within the angular sector from –72.8° to –63.2° from the nadir and the other in the horizon-to-horizon sweep. SSUSI has a 0.4° cross-track resolution in the limb-viewing section and a 0.6° resolution in the Earth-viewing section. In our modeling, we used airglow radiation values obtained strictly vertically beneath the satellite. These frames are produced every 22 s.

2. THE STATEMENT OF THE PROBLEM

We consider the statement of the problem of 2D tomography based on UV data. Our aim is to reconstruct the latitude–altitude distribution of the volume emission rate of the 135.6 nm OI ionospheric nightglow along the satellite track. The orbit parameters of

the DMSP 5D3 satellites and the SSUSI and SSULI operating modes determine the geometry of the rays that scan the reconstruction region during a satellite pass over it. This geometry is shown in the latitude–height coordinates in the top panel of Fig. 1.

The model distribution of the volume emission rate was specified by the pattern illustrated in the bottom panel of Fig. 2. This distribution qualitatively emulates the vertical profile and latitudinal variations of this parameter, incorporates the equatorial (or Appleton) anomaly (EA) and ionospheric troughs, and reflects the additional local features that we introduced into the model (thin layers below and above the *F*-layer peak height). Hereinafter, the color panels of the height–latitude distributions of the volume emission rate are presented on the unified color scale normalized to the maximum value of the model distribution.

The ionospheric airglow intensity I_k at a wavelength of 135.6 nm along the scanning direction l_k is determined by

$$\int_{l_k} \varepsilon(\phi(\mathbf{r}), h(\mathbf{r})) \exp\left(-\int \rho(\mathbf{r}') dl'\right) dl = 4\pi I_k, \quad (1)$$

where $\varepsilon(\phi(\mathbf{r}), h(\mathbf{r}))$ is the volume emission rate of the OI 135.6 nm nightglow and $\rho(\mathbf{r}')$ is the coefficient of the absorption of the 135.6 nm UV radiation in the ionosphere.

We note that the volume emission rate at 135.6 nm is linked with the distribution of the electron density [*e*] and ion and atomic oxygen concentrations [O⁺] and [O], respectively, by the following relationship [2, 14]:

$$\varepsilon = \frac{k_1 k_2 \beta_{1356} [\text{O}] [e] [\text{O}^+]}{k_2 [\text{O}^+] + k_3 [\text{O}]} + \alpha_{1356} [e] [\text{O}^+],$$

where the coefficients of the reactions k_1 , k_2 , and k_3 are approximately equal to 1.3×10^{-15} , 1.0×10^{-7} , and 1.4×10^{-10} cm³/s, respectively. The fraction of the neutralization in the excited state (O⁺S) for the emission at the wavelength of 135.6 nm is $\beta_{1356} = 0.54$ [2]; the coefficient for the radiative recombination reaction α_{1356} depends on temperature and at 1160K is approximately equal to 7.5×10^{-13} cm³/s. With the characteristic electron density, ion and atomic oxygen concentrations at the ionospheric heights, the volume emission rate at a wavelength 135.6 nm is proportional to the squared electron density. Hence, we may consider the tomographic problem (1) for the unknown distribution of electron density, as was done in a number of works [10–13]. However, the coefficient of proportionality between the volume emission rate and the square of the electron concentration may both vary with height and with time depending on the local time and season [14]. With the allowance for this, it appears reasonable to start with reconstructing the distribution of the volume emission rate $\varepsilon(\phi(\mathbf{r}), h(\mathbf{r}))$, which does not require a priori information about the physical mechanisms of a given airglow, and then reconstruct

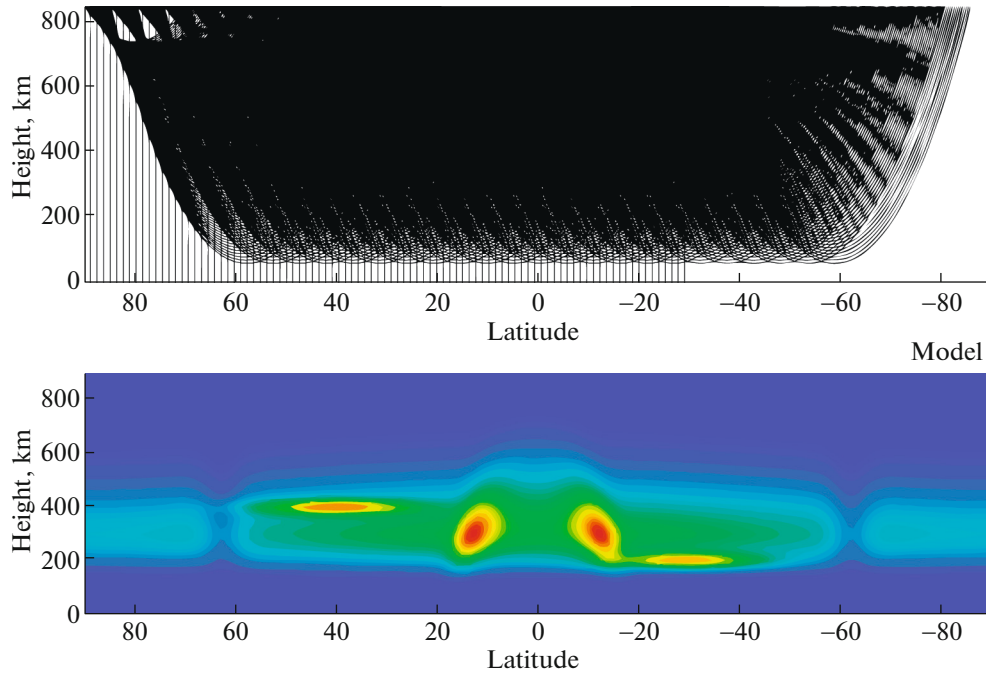


Fig. 1. Top: the ray geometry in the latitude–height coordinates; bottom: the complex model with different types of the ionospheric structures for the reconstruction.

the electron-density distribution from the obtained distribution $\varepsilon(\phi(\mathbf{r}), h(\mathbf{r}))$.

To synthesize the model data, integrals (1) are initially calculated numerically along all the scanning directions (Fig. 1, top) for the assumed model $\varepsilon = \varepsilon_{\text{mod}}(\phi, h)$ (Fig. 1, bottom). Integration is conducted by the method of rectangles along the known rays, each of which is subdivided into N_m equal intervals in the Cartesian coordinates. The resulting data $y_k = 4\pi I_k^{\text{mod}}$ are the input for the reconstruction of the volume emission rate $\varepsilon(\phi(\mathbf{r}), h(\mathbf{r}))$.

We consider the sought function under reconstruction as the decomposition in a certain finite basis $\{B\}$ with unknown numerical coefficients $\{x\}$:

$$\varepsilon(\phi, h) = \sum_{i,j} x_{i,j} B_{i,j}(\phi, h). \quad (2)$$

We use the system of the basis functions that provide bilinear interpolation of the values of the reconstructed function at the nodes of the $N_\phi \times N_h$ grid where N_ϕ and N_h are the grid dimensions along the latitude and height, respectively. Then, (1) can be cast in the following form:

$$\int_{l_k} \varepsilon(\phi(\mathbf{r}), h(\mathbf{r})) \exp\left(-\int \rho(\mathbf{r}') dl'\right) dl \approx \sum_{i,j}^{i < N_\phi, j < N_h} x_{i,j} \sum_{n=0}^{n < N_m} B_{i,j}(\phi(\mathbf{r}_n^k), h(\mathbf{r}_n^k)) \exp(-\Theta_n^k) \Delta l^k = y_k, \quad (3)$$

where $\Theta_n^k \approx \frac{1}{2} \rho(\mathbf{r}_0^k) \Delta l + \sum_{n'=1}^{n' \leq n} \rho(\mathbf{r}_{n'}^k) \Delta l^k$; $\mathbf{r}_n^k = \mathbf{R}_1^k + (\mathbf{R}_2^k - \mathbf{R}_1^k)(n + 0.5)/N_m$, $n = 0, \dots, N_m - 1$, $\Delta l^k = |\mathbf{R}_2^k - \mathbf{R}_1^k|/N_m$, and $\mathbf{R}_1^k, \mathbf{R}_2^k$ are the origin and end points of the ray l_k .

By assigning a unique index $(i, j) \rightarrow m$ to each grid node, we obtain the SLE in the coefficients of decomposition $\{x_m\}$:

$$\sum_m A_{km} x_m = y_k, \quad (4)$$

or, in the vector form with the allowance for the approximation error and data error,

$$\mathbf{A}\mathbf{x} = \mathbf{y} + \zeta. \quad (5)$$

However, we do not have rigorous models that would enable us to factor these errors in our calculations by explicitly modifying the form of the SLE. Therefore, we will instead consider the problem of minimizing the residual (4), along with paying close attention to carefully selecting the minimization algorithms. To compare the results, we will monitor the quality of the reconstruction of the model by qualitatively and quantitatively controlling the deviation of the reconstructed values from the model. To test the algorithms, one may initially neglect the contribution of the absorption in (3) and take it into account at the final stage of the analysis by using the algorithms with

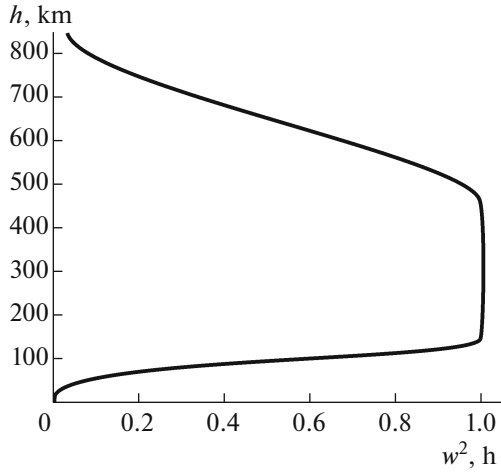


Fig. 2. The weighting function squared, $w^2(h)$.

the optimal parameters as determined at the first stage of the processing.

3. THE ALGORITHMS FOR THE SOLUTION OF SLEs

In the present work, the SLE of problem (4) was solved by the ART and SIRT iterative algorithms, which have demonstrated high efficiency in the problems of the ionospheric radio tomography [15, 16] and which are computationally efficient in solving SLEs with sparse matrices that have no special structure (diagonal or band).

The idea of the ART algorithm is to successively go through the equations of the system and for each of them to set the residual of a given equation to zero by adding a certain auxiliary vector to the solution vector. This additional vector is proportional to the line of the matrix of the SLE that specifies the given equation:

$$\mathbf{x}^{n+1} = \mathbf{x}^n + \mathbf{a}_k \frac{y_k - (\mathbf{a}_k, \mathbf{x}^n)}{(\mathbf{a}_k, \mathbf{a}_k)} \quad (6)$$

from which it directly follows that $(\mathbf{a}_k, \mathbf{x}^{n+1}) = y_k$. If the iterative sequence for the ART algorithm converges, it converges to the normal (with respect to the initial approximation) solution of the problem of finding a quasi solution to system (4).

We now consider how the same situation will be handled by the SIRT method, which has an averaging character. The additions to the solution, which were obtained for each equation in ART, in this case are initially summarized with the certain weights ρ_k and only after this are they added to the resulting solution:

$$\mathbf{x}^{n+1} = \mathbf{x}^n + \lambda \sum_k \rho_k \mathbf{a}_k \frac{y_k - (\mathbf{a}_k, \mathbf{x}^n)}{(\mathbf{a}_k, \mathbf{a}_k)}. \quad (7)$$

By specifying $\rho_k = \frac{(\mathbf{a}_k, \mathbf{a}_k)}{\|\mathbf{A}\|^2}$, we obtain the simplest and most transparent form of the SIRT algorithm:

$$\mathbf{x}^{n+1} = \mathbf{x}^n + \frac{\lambda_n}{\|\mathbf{A}\|^2} \mathbf{A}^T (\mathbf{y} - \mathbf{A} \mathbf{x}^n), \quad (8)$$

which corresponds to the natural iterative algorithm for searching for the quasi solutions of the SLE $\min \|\mathbf{A} \mathbf{x} - \mathbf{y}\|^2$.

The rate of convergence of SIRT is several orders of magnitude lower than ART (the convergence is theoretically guaranteed for $0 < \lambda_n < 2$). To achieve a faster convergence, one may specify the parameter $t_n = \frac{\lambda_n}{\|\mathbf{A}\|^2}$ by minimizing the SLE residual at each iteration.

An important property of the iterative algorithms is the possibility to control the non-negativity of the solution (volume emission rate) at each iteration step. This is achieved by setting all the negative elements \mathbf{x} to zero after each iteration step. Another useful feature of these algorithms lies in the fact that they allow the introduction of the weighting coefficients into the mathematical formulation of the problem for correcting the vertical profile of the volume emission rate. In this case, we may pass from the set of the variables \mathbf{x} to the set of the other variables $\tilde{\mathbf{x}}$, such that $x_m = \tilde{x}_m \cdot w_m$, where the weights w_m can modify the result of the reconstruction from the standpoint of the work of the ART and SIRT algorithms. By using small weights, we may suppress the artifacts of the solution in the regions where the solution should a priori be small. At the same time, in the reconstruction domains that may contain important structures of the solution, the weights should be close to unity in order to prevent the distortion of the reconstructed distribution. An example of a weighting function of this type is presented in Fig. 2.

Thus, the solution in the height interval from 150 to 450 km remains intact. Below this interval, the solution is suppressed with the approach of the ground surface (which is fairly justified from the physical standpoint), whereas above this interval the solution gradually decreases with the approach of the height of the satellite orbit (which qualitatively corresponds to the behavior of the electron density in the ionosphere).

4. THE RESULTS OF MODELING

In this section, we present the results of reconstructing the model distribution of the volume emission rate as shown in the bottom panel of Fig. 1 from the set of the modeled scanning data along the directions shown in the top panel of Fig. 1. At this step, we

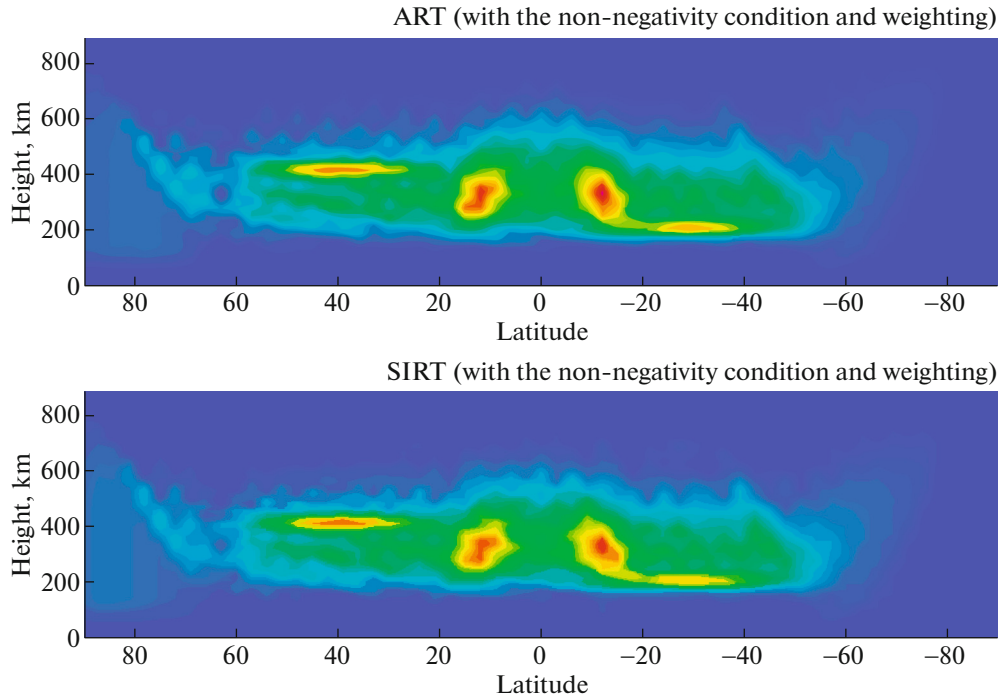


Fig. 3. Top: ART; bottom: SIRT with the condition of non-negativity and the weighting function shown in Fig. 2.

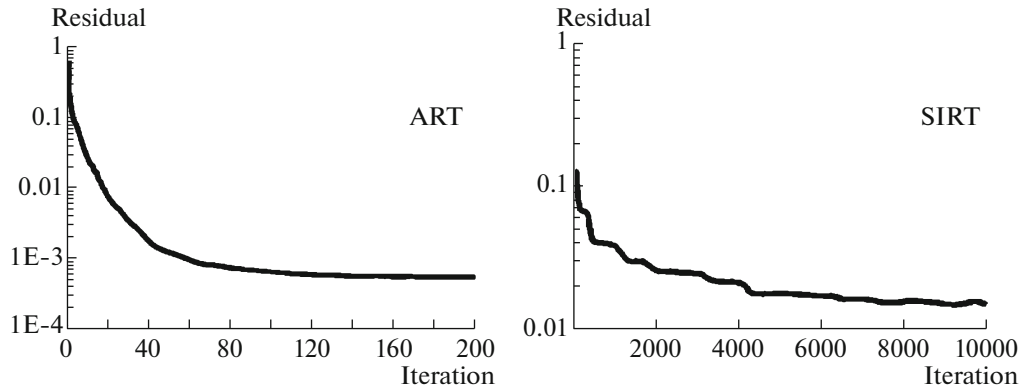


Fig. 4. The variation in the residual of SLE during the iteration process for the ART and SIRT algorithms with the non-negativity condition and the weighting function shown in Fig. 3.

disregard the absorption. The grid size $N_\phi \times N_h$ for specifying the basis function is selected at 60×60 , which is, on one hand, sufficient for resolving all the irregularities contained in the model and, on the other hand, this grid density is not higher than the density of filling the studied region by the rays (between the rays of each beam there are no void cells that are not intersected by the rays (at least by a single one)). The initial approximation is zero. The reconstruction error relative to the initial model distribution is estimated in our analysis in the norms C ($\|x\|_C = \max |x_i|$), L_1 ($\|x\|_{L_1} = \sum_i |x_i|$), and L_2 ($\|x\|_{L_2} = \sqrt{\sum_i |x_i|^2}$).

The results of the reconstructions are illustrated in Fig. 3. The convergence of the solutions in terms of the SLE residual is shown in Fig. 4. The solution reconstructed by the ART algorithm deviates from the model by $\|\epsilon - \epsilon_{\text{mod}}\|_C / \|\epsilon_{\text{mod}}\|_C = 14.3\%$, $\|\epsilon - \epsilon_{\text{mod}}\|_{L_1} / \|\epsilon_{\text{mod}}\|_{L_1} = 13.2\%$, and $\|\epsilon - \epsilon_{\text{mod}}\|_{L_2} / \|\epsilon_{\text{mod}}\|_{L_2} = 12.7\%$. The corresponding deviations of the reconstruction by SIRT are 16, 13.3, and 12.4%, respectively. It can be seen that the reconstruction reproduces the general level of the solution fairly well and captures the layout of the structures (the positions of the layers, the EA crests, and the trough in the northern hemisphere). The trough in the

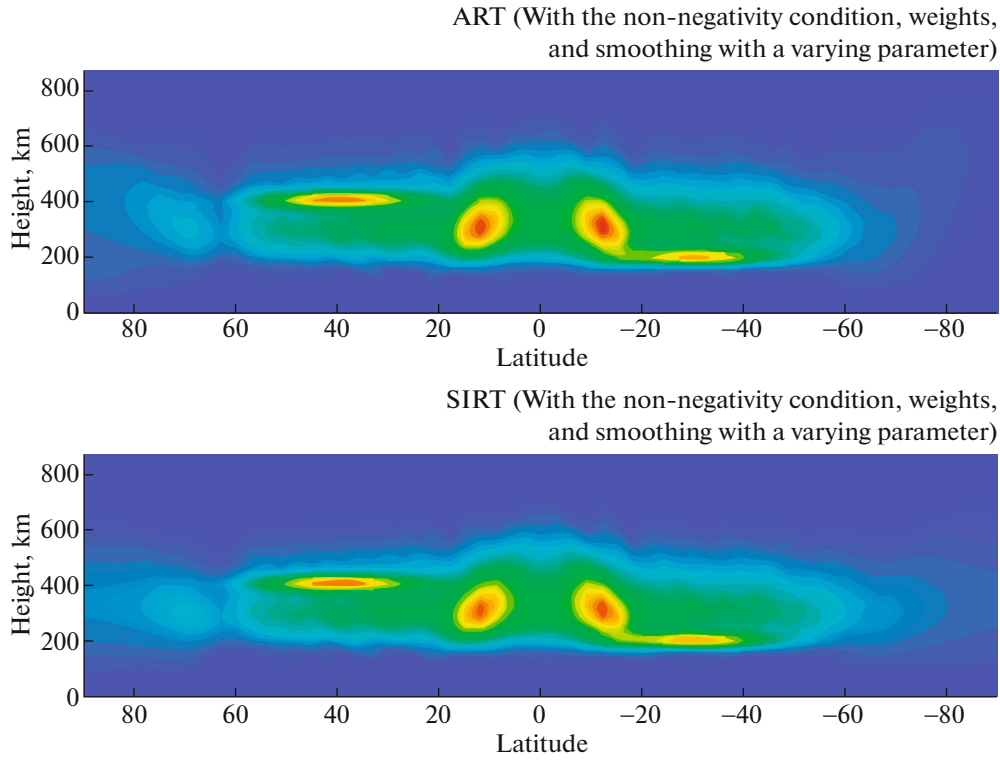


Fig. 5. Top: ART; bottom: SIRT with inter-iteration smoothing of the solution with a varying smoothing parameter.

southern hemisphere is not reconstructed due to the absence of vertical scanning rays in this latitudinal region (the model data of the SSUSI imager) (Fig. 1, top). This indicates the importance of these rays for the resolution of the method.

4.1. Inter-Iteration Smoothing of the Solution

Since with the fairly close quantitative agreement with the model, the reconstruction in Fig. 3 qualitatively differs from it mainly via the presence of the artifacts that are associated with the coarse approximation of the problem and are observed in the form of a checkerboard structure that reflects the grid structure, the next natural step to improve the reconstruction is inter-iterative smoothing of the solution. Between the successive iterations of the ART and SIRT algorithms, let us subject the solution to smoothing filtering, which averages the solution within the closest vicinity of each grid node:

$$x'_{i,j} = \sum_{i_1=i-1}^{i+1} \sum_{j_1=j-1}^{j+1} \rho_{i_1-i, j_1-j} x_{i_1, j_1}, \quad (9)$$

where

$$\rho_{i_1-i, j_1-j} = \mu_{i_1-i, j_1-j} / \sum_{i_2=i-1}^{i+1} \sum_{j_2=j-1}^{j+1} \mu_{i_2-i, j_2-j}, \quad (10)$$

and the set of the smoothing filters with the smoothing parameter p , which are symmetric by the indices and coordinates, is specified in the form:

$$\mu_{i',j'} = \mu_{i'}(p) \mu_{j'}(p), \quad \mu_{i'}(p) = \begin{cases} 1, & i' = 0, \\ p, & |i'| = 1, \end{cases} \quad (11)$$

which automatically provides the normalization (9).

We note that it is reasonable to progressively diminish the smoothing parameter p in the course of the iterations in order to prevent the contribution of the smoothing to the solution from exceeding the correction of the solution in the ART and SIRT algorithms at a given iteration step.

Figure 5 shows the results of reconstructing the model distribution with the application of inter-iteration smoothing with an exponentially decreasing parameter p . The convergence of the solutions in terms of the SLE residual is illustrated in Fig. 6. The ART- and SIRT-reconstructions in the area of comparison are visually almost indistinguishable from the model. Moreover, the final SLE residual for the SIRT reconstruction has decreased to the value that is provided by the ART algorithm. Quantitative estimation in this case gives the following figures: $\|\varepsilon - \varepsilon_{\text{mod}}\|_C / \|\varepsilon_{\text{mod}}\|_C = 6.78\%$ for ART and 7.94% for SIRT; $\|\varepsilon - \varepsilon_{\text{mod}}\|_{L_1} / \|\varepsilon_{\text{mod}}\|_{L_1} = 6.71\%$ for ART and 6.64% for SIRT; and $\|\varepsilon - \varepsilon_{\text{mod}}\|_{L_2} / \|\varepsilon_{\text{mod}}\|_{L_2} = 5.92\%$ for ART and 5.85% for SIRT.

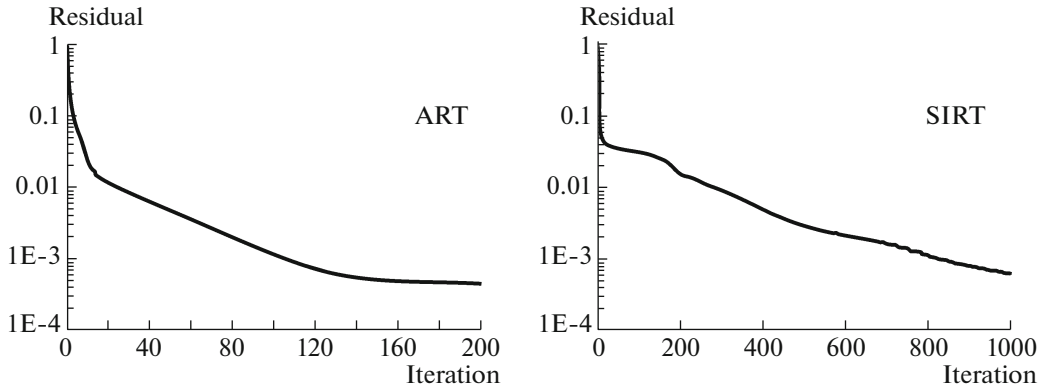


Fig. 6. The variation in the residual of SLE during the iteration process for the ART (left) and SIRT algorithms (right) with inter-iteration smoothing of the solution varying the smoothing parameter.

Hence, this indicates that a good result of the reconstruction in the problem of UV tomography with standard algorithms of the ionospheric radiotomography can be achieved if

- (1) the non-negativity of the solution is controlled at each iteration step;
- (2) weighting functions are applied for suppressing the solution in the regions where the electron density is a priori low; and
- (3) inter-iteration smoothing is used for eliminating the artifacts associated with the approximation errors with the smoothing parameter that is diminished during the iterations.

If these conditions are observed, the computational costs of the ART and SIRT algorithms are similar and the error of the reconstruction is $\sim 6\%$.

4.2. The Influence of the Noise on the Results of the Reconstruction

The results described above were obtained without artificial contamination of the data by noise. Now, having selected the optimal parameters of the algorithms of reconstruction, we may explore the implications of the noise introduced into the data for the performance of these algorithms. Let us consider this point via the example of the ART algorithm. We fix the grid size at 120×120 and the number of the iteration steps at 2000, and complicate the initial data by adding noise with a level σ that varies from 0 to 2%. We conduct reconstructions with these contaminated data and analyze the error of the solution in the norms C , L_1 , and L_2 . The results of this analysis, as shown in Fig. 7, suggest that random errors only slightly affect the results provided by the tested algorithms with the relative error in the data (the noise) within 0.5%. When the data error increases to 2%, strong noise appears in the reconstructions (Fig. 8, top), which overlaps the initial model structures, although these structures themselves remain clearly distinguishable.

The idea of smoothing can also be applied for suppressing the influence of the data errors. To do this, one should modify the smoothing algorithms in such a way as to reconcile the degree of smoothing the solution with the error in the initial data. Let the smoothing parameter p_n logarithmically vary from P_1 to P_2 in the process of iterations $n = 1, \dots, N$:

$$p_n = \exp(\ln(P_1) + (\ln(P_2) - \ln(P_1)) \times (n-1)/(N_{iter} - 1)). \quad (12)$$

As well, since the noise should be smoothed over spatial scales that are larger than the distance between the neighboring rays, the smoothing filter should be repeatedly applied to the data and the smoothing procedure should not only be conducted between the iterations but should also be executed after the last iteration.

Then, having fixed P_1 , the number of the iterations, and the number of the repeated application of the smoothing filter, by varying P_2 we may determine the value of the parameter that provides the minimal reconstruction errors. The results obtained with the

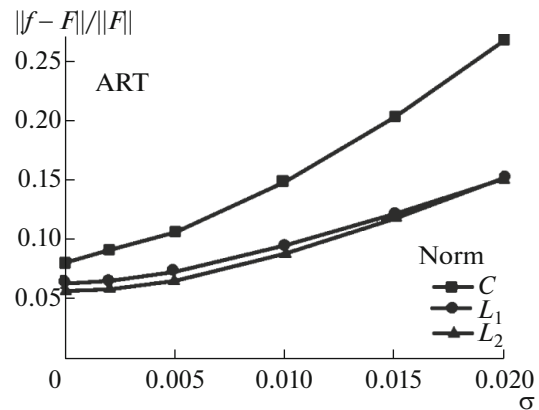


Fig. 7. The error of the ART reconstruction of the model as a function of the noise level in the data.

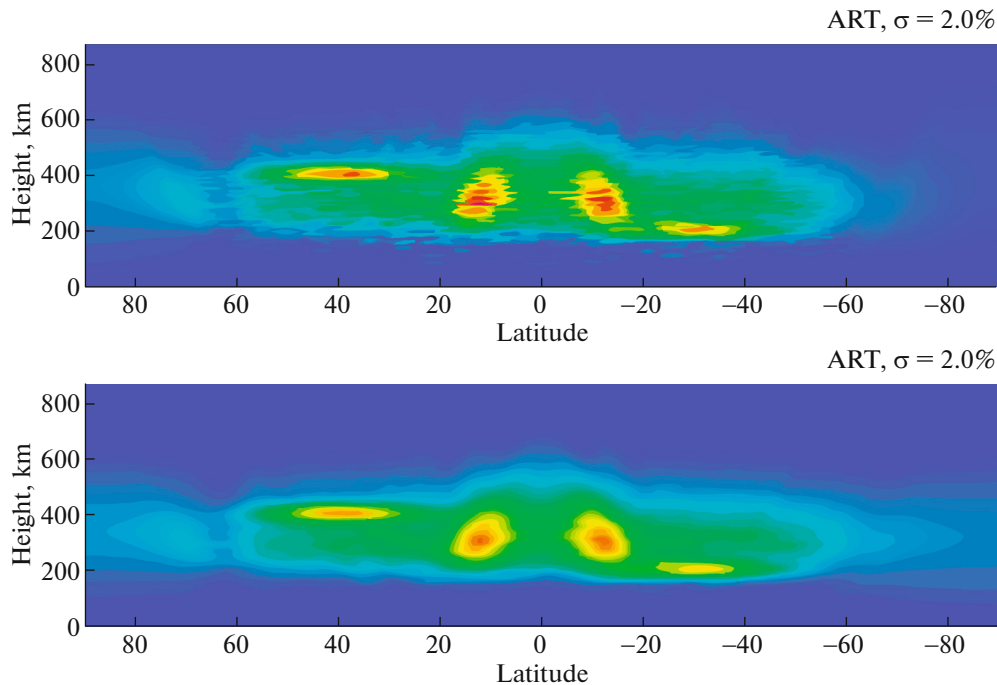


Fig. 8. The reconstruction of the model distribution from the data with the noise $\sigma = 2\%$ by the ART (top) and ART with noise suppression methods (bottom).

application of this approach for $P_1 = 0.5$ and $P_2 = 0.03$ are shown in Fig. 8 (bottom panel).

This example shows that when the error level in the initial data is known, we may a priori select the parameters of the algorithms of the reconstruction at the stage of modeling in such a way as to suppress the effects caused in the solutions by the random noise at the relative amplitude of $\sim 2\text{--}3\%$.

4.3. Allowance for Absorption

The key source of the absorption of the ionospheric airglow at a wavelength of 135.6 nm is the absorption

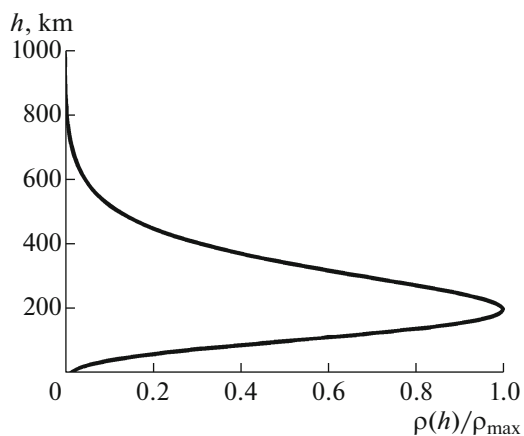


Fig. 9. The model that specifies the vertical profile of the coefficient of absorption.

by molecular oxygen in the Schumann–Runge absorption band. Hence, in the first approximation it can be assumed that the coefficient of absorption ρ only depends on height through the height dependence of the concentration of O_2 and the temperature dependence of the absorption cross section. For the purposes of modeling we assume that the vertical profile of the coefficient of absorption ρ has the shape shown in Fig. 9. In this case, the maximal value of this coefficient, ρ_{\max} , plays the role of the parameter that determines the value of absorption.

Let us consider the influence of ρ_{\max} on the quality of the reconstruction by the ART algorithm with the inter-iteration smoothing of the solution (Fig. 10). In these calculations, the grid size was 120×120 , $P_1 = 1$, $P_2 = 3 \times 10^{-6}$, and the number of the iterations was 2000. The dependence of the solution errors in the norms C , L_1 , and L_2 on the maximal value of the coefficient of absorption ρ_{\max} is illustrated by the graph in Fig. 11.

It can be seen that the distortions of the solution caused by absorption

- (a) are insignificant at $\rho_{\max} < 5 \times 10^{-7} \text{ m}^{-1}$;
- (b) become noticeable at $\rho_{\max} = 5 \times 10^{-7} \text{ m}^{-1}$; and
- (c) become large (EA is strongly asymmetric) at $\rho_{\max} = 2 \times 10^{-6} \text{ m}^{-1}$.

The influence of the absorption on the results of tomographic reconstruction becomes noticeable when for the quasi horizontal rays the contribution of the

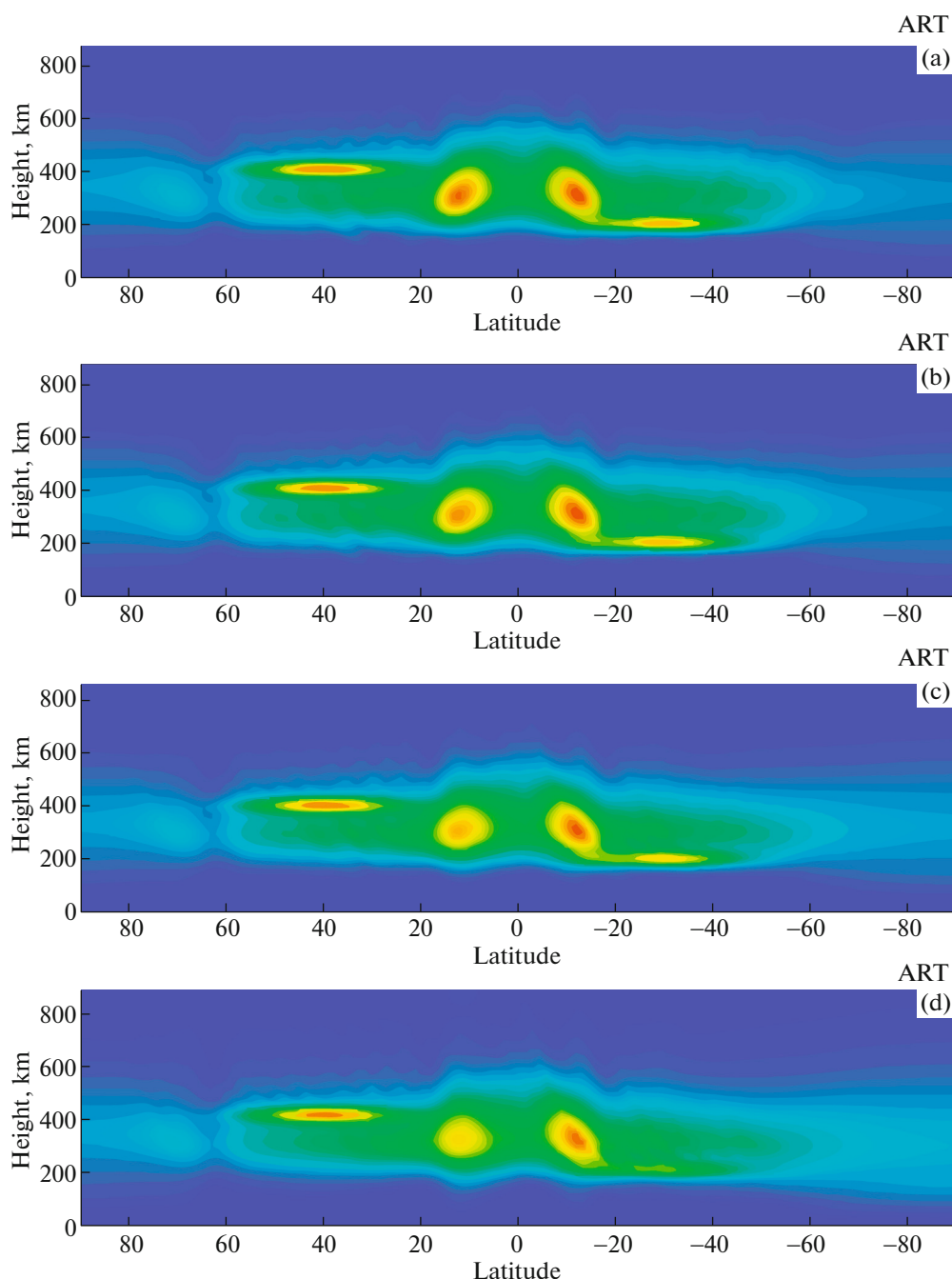


Fig. 10. ART for the problem with absorption: (a) $\rho_{\max} = 1 \times 10^{-7} \text{ m}^{-1}$; (b) $\rho_{\max} = 5 \times 10^{-7} \text{ m}^{-1}$; (c) $\rho_{\max} = 1 \times 10^{-6} \text{ m}^{-1}$; (d) $\rho_{\max} = 2 \times 10^{-6} \text{ m}^{-1}$.

integral over the second (ascending) part of the ray becomes small compared to the contribution of the integral over the first (descending) ray segment. As well as causing a partial loss of this information, this also leads to the fact that the geometry of the problem is no longer symmetrical. This, in particular, leads to asymmetry in the reconstruction of EA: the EA crest, which is inclined in the same direction as the descending parts of the rays, is reconstructed better than the

crest that is inclined identically with the ascending ray segments.

We note that at $\rho_{\max} = 2 \times 10^{-6} \text{ m}^{-1}$, the radiation intensity drops 25-fold even for the first part of the ray; at $\rho_{\max} = 1 \times 10^{-6} \text{ m}^{-1}$, the radiation intensity diminishes to one-fifth of its initial value. Clearly, such a strong absorption challenges the very idea of the tomographic reconstruction; obtaining even qualitatively reasonable results demonstrates the great poten-

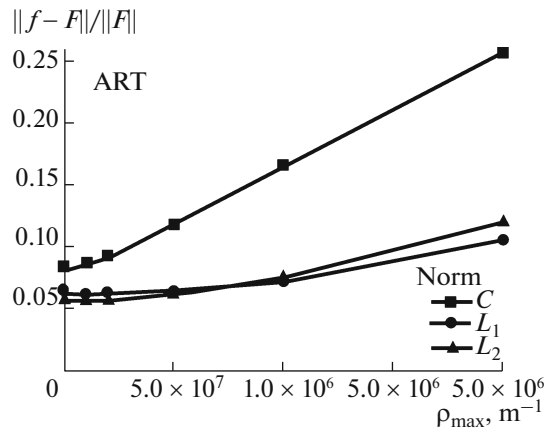


Fig. 11. The dependences of the solution error (in the C , L_1 and L_2 norms) on the maximal value of the coefficient of absorption ρ_{\max} .

tial of the developed techniques. The absorption can only be treated as small at $\rho_{\max} = 1 \times 10^{-7} \text{ m}^{-1}$, however, in this case the accuracy of the reconstruction is almost identical to that in the absence of the absorption.

CONCLUSIONS

Our numerical modeling of the problem of the ionospheric UV tomography with the real orbital geometry of the DMSP 5D3 satellites and the real operating regimes of the SSUSI and SSULI UV spectral imagers aboard these satellites shows that the distributions of the OI 135.6 nm volume emission rate in the ionosphere can be reconstructed fairly well by this method with the use of the iterative ART and SIRT algorithms, which demonstrated their efficiency in the problems of the ionospheric radio tomography. Here, the statement of the tomographic problem for the volume emission rate removes the additional difficulties associated with specifying the photochemical reactions that produce the airglow in the ionosphere (which is necessary in the case of the statement of the problem for the electron concentration). At the same time, our modeling indicates that the ART and SIRT algorithms require certain modification in order to be used for the problem of the UV ionospheric tomography. Namely, it is necessary to take the condition of the non-negativity of the solution into account, to use the weighting functions for suppressing the solution in the areas where the solution is a priori small, and to apply the inter-iteration smoothing in order to eliminate the effects of the approximation error, in which case the

smoothing parameter should be progressively diminished. As well, the analysis of the noise effects in the results of the reconstruction shows that if the noise level in the initial data is known, one may a priori select the parameters of the algorithms of reconstruction at the modeling stage in such a way as to efficiently suppress the effects of the noise with a relative amplitude of a few percent. The developed algorithms have also demonstrated their efficiency in the case of allowance for the absorption of the UV radiation in the ionosphere.

ACKNOWLEDGMENTS

The work was supported by the Russian Foundation for Basic Research (project no. 15-35-2106).

REFERENCES

1. B. A. Tinsley, A. B. Christensen, J. A. Bittencourt, et al., *J. Geophys. Res.* **78**, 1174 (1973).
2. B. A. Tinsley and J. A. Bittencourt, *J. Geophys. Res.* **80**, 2333 (1975).
3. G. T. Hicks and T. A. Chubb, *J. Geophys. Res.* **75**, 6233 (1970).
4. C. A. Barth and S. Schaffner, *J. Geophys. Res.* **75**, 4299 (1970).
5. W. C. Knudsen, *J. Geophys. Res.* **75**, 3862 (1970).
6. B. A. Tinsley, *Ann. Geophys.* **28**, 155 (1972).
7. W. H. Brune, P. D. Feldman, W. G. Anderson, et al., *Geophys. Res. Lett.* **5**, 383 (1978).
8. R. R. Meier, *Space Sci. Rev.* **58**, 1 (1991).
9. K. F. Dymond, S. E. Thonnard, R. P. McCoy, and R. H. Thomas, *Radio Sci.* **32**, 1985 (1997).
10. K. F. Dymond and R. H. Thomas, *Radio Sci.* **36**, 1241 (2001).
11. R. DeMajistre, L. J. Paxton, D. Morrison, et al., *J. Geophys. Res.: Space Phys.* **109**, A05305 (2004). doi 10.1029/2003JA010296
12. J. M. Comberiate, F. Kamalabadi, and L. J. Paxton, *Radio Sci.* **42**, RS2011 (2007).
13. E. M. McMahon, J. M. Comberiate, M. A. Kelly, and L. J. Paxton, in *Proc. 1st AIAA Atmospheric and Space Environments Conf., Texas, 2009*.
14. P. K. Rahesh, J. Y. Liu, M. L. Hsu, et al., *J. Geophys. Res.: Space Phys.* **116**, A02313 (2011). doi 10.1029/2010JA015686
15. V. Kunitsyn and E. Tereshchenko, *Ionospheric Tomography* (Springer-Verlag, 2003).
16. I. A. Nesterov and V. E. Kunitsyn, *Adv. Space Res.* **47**, 1789 (2011).

Translated by M. Nazarenko